Sound Radiation from Railway Wheels including Ground Reflections: A half-space formulation for the Fourier Boundary Element Method

Journal of Sound and Vibration 493 (2021) 115822

Contents lists available at ScienceDirect

Journal of Sound and Vibration

journal homepage: www.elsevier.com/locate/jsv

Sound radiation from railway wheels including ground reflections: A half-space formulation for the fourier boundary element method

François Fabre, Jannik S. Theyssen*, Astrid Pieringer, Wolfgang Kropp

Chalmers University of Technology, Division of Applied Acoustics, Department of Architecture and Civil Engineering, Sven Hultins Gata 8a, Gothenburg 41258, Sweden

ARTICLE INFO

Article history:
Received 25 February 2020
Revised 7 October 2020
Accepted 31 October 2020
Available online 2 November 2020

Keywords:
Axisymmetry
Waveguide FEM
Green's functions
Radiation Efficiency
Railway Wheel
Slab Track

ABSTRACT

Current models for the acoustic radiation from railway wheels assume free field radiation. However, slab tracks are increasingly used for new railway lines. The acoustically hard surface of those tracks makes a re-evaluation of the free field assumption relevant, as such a surface can affect the radiation efficiency of an acoustic radiator. The wheel as the acoustic radiator is most conveniently described in a cylindrical coordinate system, thus making use of its axisymmetry. While this is a viable solution for the structural vibrations, for instance by using the curved Waveguide Finite Element formulation, the axisymmetry breaks when including a reflective plane in the calculation of the acoustic radiation. A convenient method to include an infinitely large, reflective plane is by using half-space Green's functions in combination with the Boundary Element method. This method can be formulated in cylindrical coordinates using the Fourier series BEM (FBEM). However, the FBEM has not yet been combined with half-space Green's functions. This paper provides a half-space formulation for the FBEM, which enables e.g. the evaluation of sound radiation of railway wheels over reflective surfaces. Finally, it is shown that the assumption of free field radiation for railway wheels is valid, as there is no major contribution of the reflective plane to the radiation efficiency of the wheel. The developed method is validated against laboratory measurements as well as analytical models.

1. Introduction

A solid has axial symmetry when it can be created by rotating a planar geometry around an axis. The axisymmetry of objects is often used to downscale numerical models, as simplifying the geometry to its planar representation considerably decreases the degrees of freedom in the system. The comparatively more elaborate element formulation of axisymmetric elements pays off in decreased calculation times. This downscaling is utilised in the following for calculating both structural vibrations as well as sound radiation. Standard axisymmetric finite elements are well established, see e.g. [1], and part of most standard finite element packages [2,3].

However, there is a large body of research using a curved waveguide finite element (WFE) formulation for axisymmetric bodies, especially in the field of predicting tyre vibrations and noise [4–7]. A summary of the curved WFE method can be

* Corresponding author.
E-mail address: jannik.theyssen@chalmers.se (J.S. Theyssen).

https://doi.org/10.1016/j.jsv.2020.115822

found in [8]. In this paper, this WFE method is used for calculating the structural response of railway wheel, which is a novel application of this method.

At least three methods have been used to calculate the sound radiation from axisymmetric structures. Firstly, in [6,7], the surface velocities are translated into a Cartesian coordinate system. Then, an implementation based on the standard 3D boundary element method (BEM) and half-space Green's functions developed in [9] is used. The inherent benefit of applying BEM on external problems, in which the structure radiates into the surrounding air, is that the Sommerfeld radiation condition [10] is fulfilled. Using BEM, the sound intensity is calculated on a half-sphere enclosing the wheel and the reflective ground plane. However, the computational cost is comparatively high due to the necessary meshing of the 3D surface of the vibrating object.

Secondly, in [5], a curved WFE model is used for calculating the structural vibrations. By introducing coupling elements between the structure and the surrounding air into the WFE model, the axisymmetry can be utilised even for the sound radiation. However, to fulfil the Sommerfeld radiation condition, a perfectly matched layer needs to be used, see e.g. [11].

The third approach, which this paper builds on, combines the benefits of an axisymmetric formulation and the BEM. Here, the acoustic variables of the problem are expanded as a Fourier series, which is why the method is often referred to as the Fourier series BEM (FBEM). The method is based on a paper by Seybert et al. [12], building on earlier research by Meyer et al. [13]. As will be shown in Section 2.2, the drawback of the FBEM formulation is that numerical difficulties occur in the evaluation of the combination of Fourier Transform and generator based integrals, as these integrals can be singular and oscillatory [14]. The management of these singularities has been attempted using elliptic integrals by Soenarko et al. [15] and Juhl [16]. A major advancement of the method was proposed by Kuijpers et al. [14]. The fact that certain integrals can be calculated using the numerically efficient Fast Fourier Transform (FFT), instead of an integration scheme based on Gaussian quadrature, leads to a major reduction in the calculation time. Note that all methods that make use of the axisymmetry assume sound radiation into free space.

The sound radiation from railway wheels has been found to be one of the major contributors to overall railway noise and has been subject to extensive research [17–20]. In [19], the vibration behaviour of the railway wheel is described by its eigenmodes, which are characterised by their number of nodal diameters and nodal circles. Physically, this is close to the idea of FBEM, such that each order in the Fourier expansion corresponds to a number of nodal diameters on the structure. At the same place it is pointed out that modes of order two and above have the largest contribution to rolling noise.

An engineering model for the sound radiation has been developed by Thompson and Jones [20]. There, the axle geometry is neglected for vibration and radiation, using a fixed constraint at the wheel hub. According to [19], this produces adequate results starting from circumferential mode order 2. In that study, an axisymmetric BE formulation, corresponding to the third approach, is used to analyse the radiation ratio and directivity of wheels with different geometries. This radiation ratio is then evaluated for different modes and numbers of nodal diameters. In [21], the engineering model is compared to the 3D BEM implementation developed in [22] and a good agreement is found. Both Sheng et al. [23] and Zhong et al. [24] use a similar approach as in [20] to calculate the sound radiation from high-speed railway wheels. Especially the influence of the rotating excitation force is studied here.

Reflecting on the presented methods, it is clear that so far there is only the possibility of including a reflective plane when disregarding the benefits of an axisymmetric formulation. This paper presents a method using half-space Green's functions in the FBEM, which enable the calculation of the sound radiation of axisymmetric bodies in cylindrical coordinates over a hard reflective ground plane. Considerations regarding the accuracy of this method are presented. This paper then combines the WFE and FBE method for the application on a railway wheel. To the authors' knowledge, these methods have not been combined before and so a validation based on laboratory measurements and analytical models will be given.

2. Method

In the following, the waveguide finite element method as well as the boundary element method for axisymmetric bodies are summarised. A half-space formulation for solving the acoustic radiation problem in Fourier-expanded cylindrical coordinates is introduced. Considerations regarding its efficiency are presented and a validation of the method is shown.

2.1. WFE formulation

A summary of the method is stated here for convenience. A comprehensive overview can be found in [6,8]. Describing the three-dimensional geometry by its constant cross-section enables the use of a two dimensional element formulation and drastically reduces the degrees of freedom in the system. The cross-section is defined in the (x, r)-plane with the radial direction r. The behaviour in the third dimension, which in case of an axisymmetric body refers to the circumferential direction θ, is described by propagating, decaying waves.

The displacement $\boldsymbol{u}$ at any location on the discretised body is described by

$$\boldsymbol{u}(x, r, \theta) = \underline{\mathbf{N}}(\xi, \eta)\mathbf{u}(\theta) \tag{1}$$

with $\underline{\mathbf{N}}(\xi, \eta)$ a matrix whose entries are shape functions N_i and $\mathbf{u}$ containing all nodal displacements. For elastic materials without viscosity, Hamilton's principle is written

$$\delta L = \delta(U - K + A) = 0 \tag{2}$$

with the Lagrangian L, the total strain energy U, the kinetic energy K and the potential energy of the loading A, where δ denotes "the first variation of". For a harmonic motion, Eq. (2) can be rewritten as

$$\delta L = \delta \int_V \left(\boldsymbol{\epsilon}^H \mathbf{D} \boldsymbol{\epsilon} - \rho\omega^2 \boldsymbol{u}^H \boldsymbol{u} - \boldsymbol{u}^H \boldsymbol{f}\right) \mathrm{d}V \tag{3}$$

with the volume of the structure V, the material stiffness matrix $\mathbf{D}$ and density ρ. The variable ω represents the circular frequency and $\boldsymbol{f}$ is an external force density. The superscript ^{H} denotes the complex conjugate transpose.

The material strain vector $\boldsymbol{\epsilon}$ can be expressed on element e in terms of the nodal displacements $\mathbf{u}_e$

$$\boldsymbol{\epsilon} = \left(\mathbf{E}_0 + \mathbf{E}_1 \frac{\partial}{\partial\theta}\right) \mathbf{u}_e \tag{4}$$

as shown in Appendix A. Using this definition, Hamilton's principle can be reformulated to

$$\delta L = \int_0^{2\pi} \left(\sum_{m=0}^{1} \sum_{n=0}^{1} \frac{\partial^n \delta \mathbf{u}^H}{\partial\theta^n} \mathbf{A}_{mn} \frac{\partial^m \mathbf{u}}{\partial\theta^m} - \omega^2 \delta \mathbf{u}^H \mathbf{M} \mathbf{u} - \delta \mathbf{u}^H \mathbf{f} \right) \mathrm{d}\theta \tag{5}$$

with the stiffness and mass matrix $\mathbf{A}_{mn}$ and $\mathbf{M}$ and the weighted force vector $\mathbf{f}$, respectively, which are obtained by solving $\mathbf{a}_{e,mn}$, $\mathbf{m}_e$ and $\mathbf{f}_e$ for each element and assembling to the global matrices and vector

$$\mathbf{a}_{e,mn} = \int_{S_e} \mathbf{E}_n{}^T \mathbf{D} \mathbf{E}_m \; r \mathrm{d}r\mathrm{d}x \tag{6}$$

$$\mathbf{m}_e = \int_{S_e} \mathbf{N}^T \rho \mathbf{N} \; r \mathrm{d}r\mathrm{d}x \tag{7}$$

and

$$\mathbf{f}_e = \int_{S_e} \mathbf{N}^T \boldsymbol{f} \; r \mathrm{d}r\mathrm{d}x \tag{8}$$

with S_e the surface of the element. The integral and the 'first variation of' vanishes after integration by parts of δL with respect to the θ-coordinate. The equation of motion is expressed in spatial and wavenumber domain as follows,

$$\left(\mathbf{K}_2 \frac{\partial^2}{\partial\theta^2} + \mathbf{K}_1 \frac{\partial}{\partial\theta} + \mathbf{K}_0 - \omega^2 \mathbf{M}\right) \mathbf{u}(\theta) = \mathbf{f}(\theta) \tag{9}$$

$$\left(\mathbf{K}_2 (-\mathrm{j}\kappa)^2 + \mathbf{K}_1 (-\mathrm{j}\kappa) + \mathbf{K}_0 - \omega^2 \mathbf{M}\right) \mathbf{u}(\kappa) = \mathbf{f}(\kappa) \tag{10}$$

with $\mathbf{K}_2 = -\mathbf{A}_{11}$, $\mathbf{K}_1 = \mathbf{A}_{01} - \mathbf{A}_{10}$ and $\mathbf{K}_0 = \mathbf{A}_{00}$.

Since only integer wavenumbers can propagate in circumferential direction, it is possible to prescribe the wavenumber κ and solve the resulting linear eigenvalue problem for ω. Physically, this corresponds to solving for the cross-sectional modes of the body for each circumferential order. Assuming the equation system is solved for N circumferential orders and S cross-sectional modes are obtained for each order, then each mode at eigenfrequency $\omega_{n,s}$ is described by the corresponding eigenvector $\mathbf{U}_{n,s}$. The nodal displacement $\mathbf{u}$ for each circumferential order can be obtained by modal superposition [6, Ch. 4],

$$\mathbf{u}(\theta, \omega) = \sum_{n=-N}^{N} \sum_{s=1}^{S} \frac{\mathbf{U}_{n,s}^H \mathbf{F}_n(\omega)}{\left((1 + \mathrm{j}\eta(\omega))\omega_{n,s}^2 - \omega^2\right) m_{n,s}} \mathbf{U}_{n,s} \mathrm{e}^{-\mathrm{j}n\theta} \tag{11}$$

with the loss factor η and the modal mass $m_{n,s}$

$$\delta_{s,t} m_{n,s} = \mathbf{U}_{n,s}^H \mathbf{M} \mathbf{U}_{n,t} \tag{12}$$

in which $\delta_{s,t}$ is the Kronecker delta.

The nodal displacements of the FE-nodes at the boundary of the structure can be projected on the boundary normal direction at each node. Multiplication with $\mathrm{j}\omega$ produces the surface normal velocity which serves as the input to the boundary element calculation.

2.2. FBEM Formulation

The Kirchhoff-Helmholtz integral equation describes the relation of the pressure amplitude on a boundary to the pressure field in a surrounding fluid. It is the basis for the Boundary Element Method (BEM) and is expressed as

$$c(\mathbf{r}) p(\mathbf{r}) = \int_S \left(G(\mathbf{r}; \mathbf{r_0}) \partial_{\mathbf{n}} p(\mathbf{r_0}) - \partial_{\mathbf{n}} G(\mathbf{r}; \mathbf{r_0}) p(\mathbf{r_0}) \right) \mathrm{d}S_0 \tag{13}$$

$$s = -\int_S \left(\mathrm{j}\rho\omega \; G(\mathbf{r}; \mathbf{r_0}) v_n(\mathbf{r_0}) + \partial_{\mathbf{n}} G(\mathbf{r}; \mathbf{r_0}) p(\mathbf{r_0}) \right) \mathrm{d}S_0 \tag{14}$$

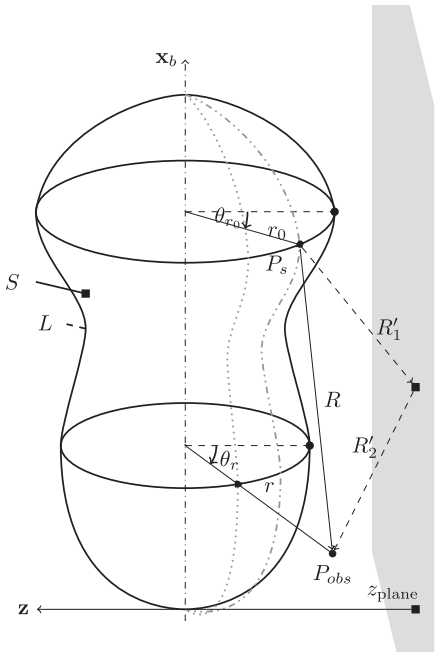

Fig. 1. Axisymmetric body over a reflecting plane. R is the path length between the source position P_s and the observer position P_{obs}. Notice the total reflected path length is $R' = R_1' + R_2'$. The surface S is created by rotating the generator L around the symmetry axis. z_{plane} is the z-coordinate of the intersection of the plane and with z-axis. The z-axis is oriented normal both to the plane and the symmetry axis.

with the Green's function of the considered problem $G(\mathbf{r}; \mathbf{r_0})$, the pressure $p(\mathbf{r_0})$ and surface normal velocity $v_n(\mathbf{r_0})$ at a source point P_s on the boundary S, the density of the fluid ρ. The symbol $\partial_{\mathbf{n}}$ represents the derivative with respect to the outgoing normal direction on the fluid boundary $\mathbf{n}$. The coefficient $c(\mathbf{r})$ is $1/2$ for an observer point P_{obs} on a smooth boundary, 1 in the fluid and 0 otherwise.

The Fourier Boundary Element Method (FBEM) utilises the axisymmetry of a body similar to WFEM, assuming that the sound field in circumferential direction can be described by a superposition of circumferential orders and therefore expanded in Fourier series. However, the reflection from a non axisymmetric plane is not easily described in this cylindrical coordinate system. The following sections present the necessary steps leading to the numerical implementation of half-space Green's functions in cylindrical coordinates described by the basis vectors $(\mathbf{x}_b, \mathbf{r}_b, \theta_b)$.

2.2.1. FBEM formulation of the physical quantities

Consider the arbitrary axisymmetric body shown in Fig. 1 radiating over an infinite plane with a given reflection coefficient R_p.

In cylindrical coordinates the half space Green's function G_{hs} is

$$G_{hs}(\mathbf{r}, \mathbf{r}_0) = \underbrace{\frac{\mathrm{e}^{-\mathrm{j}kR}}{4\pi R}}_{G(\mathbf{r}, \mathbf{r}_0)} + \underbrace{R_p \frac{\mathrm{e}^{-\mathrm{j}kR'}}{4\pi R'}}_{G_r(\mathbf{r}, \mathbf{r}_0)} \tag{15}$$

with the first term corresponding to the free field Green's function and the second term describing the reflected field. Notice that this simplified formulation of the half-space Green's function is only a valid approximation for three special cases: (i) an infinite normal impedance at the boundary, i.e. $R_p = 1$, and (ii) for a perfectly soft boundary, i.e. $R_p = -1$ [9]. The trivial case (iii) $R_p = 0$ describes the situation in which no boundary is present.

The distances R and R' are written

$$R = \|\mathbf{r} - \mathbf{r_0}\| = \sqrt{(x - x_0)^2 + (r - r_0)^2 + 2rr_0(1 - \cos(\theta_r - \theta_{r_0})} \tag{16}$$

and

$$R' = \sqrt{(x - x_0)^2 + (r - r_0)^2 + 2rr_0(1 + \cos(\theta_r + \theta_{r_0})) + 4z_{\text{plane}}\left(r\cos(\theta_r) + r_0\cos(\theta_{r_0}) + z_{\text{plane}}\right)} \tag{17}$$

with the wavenumber k in circumferential direction.

The surface integral in Eq. (14) becomes $\mathrm{d}S_0 = r_0\ \mathrm{d}l_0\mathrm{d}\theta_{r_0}$, where $\mathrm{d}l_0$ represents a line segment on the generator L. The necessary circumferential periodicity of all variables leads to the Fourier expansion

$$\begin{aligned} p(\mathbf{r}) &= \sum_{m=-\infty}^{\infty} P_m^*(x,r)\mathrm{e}^{-\mathrm{j}m\theta_r}, \\ p(\mathbf{r_0}) &= \sum_{m=-\infty}^{\infty} P_m(x_0,r_0)\mathrm{e}^{-\mathrm{j}m\theta_{r_0}}, \\ v_n(\mathbf{r_0}) &= \sum_{m=-\infty}^{\infty} V_m(x_0,r_0)\mathrm{e}^{-\mathrm{j}m\theta_{r_0}} \end{aligned} \tag{18}$$

with

$$\begin{aligned} P_m^*(x,r) &= \frac{1}{2\pi}\int_0^{2\pi} p(\mathbf{r})\mathrm{e}^{\mathrm{j}m\theta_r}\mathrm{d}\theta_r, \\ P_m(x_0,r_0) &= \frac{1}{2\pi}\int_0^{2\pi} p(\mathbf{r_0})\mathrm{e}^{\mathrm{j}m\theta_{r_0}}\mathrm{d}\theta_{r_0}, \\ V_m(x_0,r_0) &= \frac{1}{2\pi}\int_0^{2\pi} v_n(\mathbf{r_0})\mathrm{e}^{\mathrm{j}m\theta_{r_0}}\mathrm{d}\theta_{r_0} \end{aligned} \tag{19}$$

in which the subscript * denotes that P_{obs} can be located both on the boundary and in the domain. The reflected field $G_r(\mathbf{r},\mathbf{r_0})$ can not be directly expanded on $\theta_r - \theta_{r_0}$. A 2D Fourier Transform has to be applied on $G_r(\mathbf{r},\mathbf{r_0})$ such that $G_{hs}(\mathbf{r},\mathbf{r_0})$ writes

$$G_{hs}(\mathbf{r},\mathbf{r_0}) = \frac{1}{2\pi}\left(\sum_p H_p\mathrm{e}^{-\mathrm{j}p(\theta_r-\theta_{r_0})} + \sum_{m,n} H_{r_{nm}}\mathrm{e}^{-\mathrm{j}(n\theta_r - m\theta_{r_0})}\right) = \frac{1}{2\pi}\sum_m\left(H_m\mathrm{e}^{-\mathrm{j}m\theta_r} + \sum_n H_{r_{nm}}\mathrm{e}^{-\mathrm{j}n\theta_r}\right)\mathrm{e}^{\mathrm{j}m\theta_{r_0}} \tag{20}$$

with the coefficients H_m and $H_{r_{nm}}$, which are dependent on x, r, x_0 and r_0,

$$\begin{aligned} H_m &= \frac{1}{2\pi}\int_0^{2\pi} 2\pi\ G(\mathbf{r};\mathbf{r_0})\mathrm{e}^{\mathrm{j}m(\theta_r-\theta_{r_0})}\ \mathrm{d}(\theta_r-\theta_{r_0}) \\ H_{r_{nm}} &= \frac{1}{4\pi^2}\int_0^{2\pi}\int_0^{2\pi} 2\pi\ G_r(\mathbf{r},\mathbf{r_0})\mathrm{e}^{\mathrm{j}(n\theta_r - m\theta r_0)}\mathrm{d}\theta_r\mathrm{d}\theta_{r_0}. \end{aligned} \tag{21}$$

Analogously,

$$\partial_{\mathbf{n}} G_{hs}(\mathbf{r},\mathbf{r_0}) = \frac{1}{2\pi}\sum_m\left(H'_m\mathrm{e}^{-jm\theta_r} + \sum_n H'_{r_{nm}}\mathrm{e}^{-\mathrm{j}n\theta_r}\right)\mathrm{e}^{\mathrm{j}m\theta_{r_0}} \tag{22}$$

where the coefficients H'_m and $H'_{r_{nm}}$ are the derivatives of H_m and $H_{r_{nm}}$ and dependent on x, r, x_0 and r_0,

$$\begin{aligned} H'_m &= \frac{1}{2\pi}\int_0^{2\pi} 2\pi\,\partial_{\mathbf{n}} G(\mathbf{r};\mathbf{r_0})\mathrm{e}^{\mathrm{j}m(\theta_r-\theta_{r_0})}\ \mathrm{d}(\theta_r-\theta_{r_0}), \\ H'_{r_{nm}} &= \frac{1}{4\pi^2}\int_0^{2\pi}\int_0^{2\pi} 2\pi\,\partial_{\mathbf{n}} G_r(\mathbf{r},\mathbf{r_0})\mathrm{e}^{\mathrm{j}(n\theta_r - m\theta r_0)}\mathrm{d}\theta_r\mathrm{d}\theta_{r_0}. \end{aligned} \tag{23}$$

At this point, solving $p(x,r,\theta_r)$ is equivalent to solving $P_m^*(x,r)$ for every order m. This means that the initial 3D problem can be replaced by an infinite sum of 2D boundary problems if the the Fourier coefficient amplitudes are known.

2.2.2. Rewriting of the Kirchhoff-Helmholtz integral equation

For clarity, Fourier coefficients are now written without their spatial dependencies. Inserting Eq. (18), Eq. (20) and Eq. (22) in the integral formulation Eq. (14) leads to

$$c(\mathbf{r})\sum_m P_m^*\mathrm{e}^{-\mathrm{j}m\theta_r} = -\frac{1}{2\pi}\int_S\sum_{\mathrm{p,m}}\left[\mathrm{j}\rho\omega\left(\mathrm{H_m e^{-jm\theta_r}} + \sum_{\mathrm{n}}\mathrm{H_{r_{nm}} e^{-jn\theta_r}}\right)\mathrm{V_p} + \left(\mathrm{H'_m e^{-jm\theta_r}} + \sum_{\mathrm{n}}\mathrm{H'_{r_{nm}} e^{-jn\theta_r}}\right)\mathrm{P_p}\right]\mathrm{e}^{-\mathrm{j(p-m)}\theta_{r_0}}\,\mathrm{dS_0} \tag{24}$$

where the orthogonality property between complex exponentials can be used. The integral over θ_{r_0} yields $m = n$, therefore

$$\begin{aligned} c(\mathbf{r})\sum_m P_m^*\mathrm{e}^{-\mathrm{j}m\theta_r} &= -\int_L\sum_p\left[\mathrm{j}\rho\omega\left(H_p\mathrm{e}^{-\mathrm{j}p\theta_r} + \sum_n H_{r_{np}}\mathrm{e}^{-\mathrm{j}n\theta_r}\right)V_p + \left(H'_p\mathrm{e}^{-\mathrm{j}p\theta_r} + \sum_n H'_{r_{np}}\mathrm{e}^{-\mathrm{j}n\theta_r}\right)P_p\right]r_0\mathrm{d}l_0 \\ &= -\int_L\sum_p\left[\left(\mathrm{j}\rho\omega H_p V_p + H'_p P_p\right)\mathrm{e}^{-\mathrm{j}p\theta_r} + \sum_{\mathrm{n}}\left(\mathrm{j}\rho\omega\mathrm{H_{r_{np}}V_p} + \mathrm{H'_{r_{np}}P_p}\right)\mathrm{e}^{-\mathrm{jn}\theta_r}\right]\mathrm{r_0 dl_0} \end{aligned} \tag{25}$$

With that, the Fourier Boundary Integral equation can be expressed in a 3D half-space as

$$c(\mathbf{r})P_m^* = -\int_L \left[\underbrace{\mathrm{j}\rho\omega H_m V_m + H'_m P_m}_{\text{Direct field contribution}} + \underbrace{\sum_p \left(\mathrm{j}\rho\omega H_{r_{mp}} V_p + H'_{r_{mp}} P_p\right)}_{\text{Reflected field contribution}} \right] r_0 \mathrm{d}l_0. \tag{26}$$

which can be written as

$$\frac{1}{2}P_m = -\int_L \left[\mathrm{j}\rho\omega H_m V_m + H'_m P_m + \sum_p \left(\mathrm{j}\rho\omega H_{r_{mp}} V_p + H'_{r_{mp}} P_p\right) \right] r_0 \mathrm{d}l_0 \tag{27}$$

if the observer point P_{obs} is located on a smooth boundary. The efficiency of the calculation of H_m, H'_m, $H_{r_{mp}}$ and $H'_{r_{mp}}$ is fundamental to this method and is discussed in the following subsection.

2.2.3. Fast fourier transform computations

H_m and H'_m can be evaluated numerically by means of Gaussian quadrature. However, since they need to be computed for each order, Kuijpers [14] proposed a method using the Fast Fourier Transform (FFT) algorithm, enabling the computation of all necessary orders at once. An expression for the minimum required number of Fourier samples n_{FFT} for the circumferential coordinate $\theta_r - \theta_{r_0}$ is proposed to evaluate the free field contribution $G(\mathbf{r}, \mathbf{r_0})$ in the Green's function. A relative error not exceeding 10^{-3} is obtained in [14] with the expression

$$n_{\mathrm{FFT}}(\mathbf{r}, \mathbf{r_0}) = 14\left(c_s + \frac{c_o}{2\pi}\right)^{0.9} \tag{28}$$

with

- $c_s = \dfrac{R_{\max}}{R_{\min}}$, a steepness criteria describing the slope of $G(\mathbf{r}, \mathbf{r_0})$ near $\theta_r = \theta_{r_0}$,
- $c_o = k(R_{\max} - R_{\min})$, an oscillation criteria describing the impact of $\mathrm{e}^{-\mathrm{j}kR}$ for high frequencies and/or large difference $(R_{\max} - R_{\min})$.

$R_{\max}$ and $R_{\min}$ are, respectively, the maximum and the minimum distance between $P_{obs}(\theta_r)$ and $P_s(\theta_{r_0})$ when considering every possible difference $(\theta_r - \theta_{r_0})$. Once $G(\mathbf{r}, \mathbf{r_0})$ is known for a given couple source/observer points for n_{FFT} values, one can obtain H_m by selecting the coefficient at the sought position in the FFT. The same process is applied to $\partial_{\mathbf{n}} G(\mathbf{r}, \mathbf{r_0})$ to get H'_m.

This approach has been adapted for the calculation of the 2D Fourier Transform of $G_r(\mathbf{r}, \mathbf{r_0})$. Since $G_r(\mathbf{r}, \mathbf{r_0})$ is of the same form as $G(\mathbf{r}, \mathbf{r_0})$, the same criteria can be used to evaluate the minimum number of Fourier Transform samples for each angle ($n_{\mathrm{FFT},r}$ and n_{FFT,r_0}) for a given accuracy. The steepness and oscillation criteria for the Fourier Transform over θ_r are noted $c_{s,r}$ and $c_{o,r}$ while the one over θ_{r_0} are noted c_{s,r_0} and c_{o,r_0}.

Fig. 2 shows the function $G_r(\mathbf{r}, \mathbf{r_0})$ over both angular coordinates. It is apparent that e.g. for a transformation over θ_r, the slope of $G_r(\mathbf{r}, \mathbf{r_0})$ varies depending on the value of θ_{r_0}. Thus, the criteria are functions of θ_{r_0} and write $c_{s,r}(\theta_{r_0}) = R'_{r,\max}(\theta_{r_0})/R'_{r,\min}(\theta_{r_0})$ and $c_{o,r}(\theta_{r_0}) = k(R'_{r,\max}(\theta_{r_0}) - R'_{r,\min}(\theta_{r_0}))$. $R'_{r,\max}(\theta_{r_0})$ and $R'_{r,\min}(\theta_{r_0})$ are, respectively, the relative maximum and minimum of R' when varying θ_r as shown in Fig. 3. In order to obtain an expression for $n_{\mathrm{FFT},r}(c_{s,r}, c_{o,r}) = n_{\mathrm{FFT},r}(\theta_{r_0})$, $G_r(\mathbf{r}, \mathbf{r_0})$ is computed for a large number of pairs of source and observer points so that $c_{s,r} \in [1, 9]$ and $c_{o,r} \in [0, 160]$. These ranges correspond to realistic scenarios when solving on the boundary of a body such as a train wheel in the frequency range [0, 10000] Hz. The Fourier Transform over θ_r is computed by Gaussian quadrature for circumferential

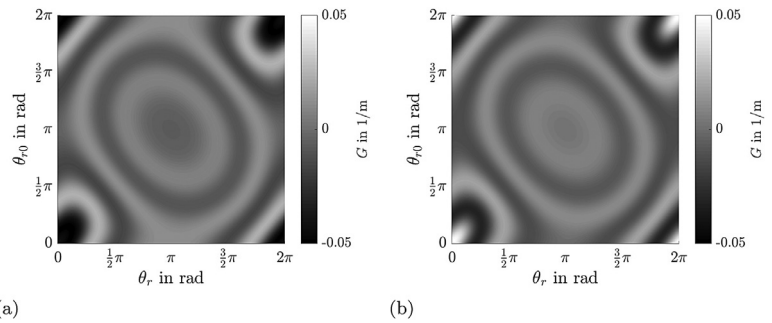

Fig. 2. Example of the θ_r/θ_{r_0}-dependency of the Green's function for a given geometric situation. (a) real and (b) imaginary part of the Green's function for $\mathbf{r} = (0\mathrm{m}, 3\mathrm{m}, [0, 2\pi])$, $\mathbf{r_0} = (1\mathrm{m}, 2.5\mathrm{m}, [0, 2\pi])$, $z_{\mathrm{plane}} = -3.1\mathrm{m}$ at 100 Hz.

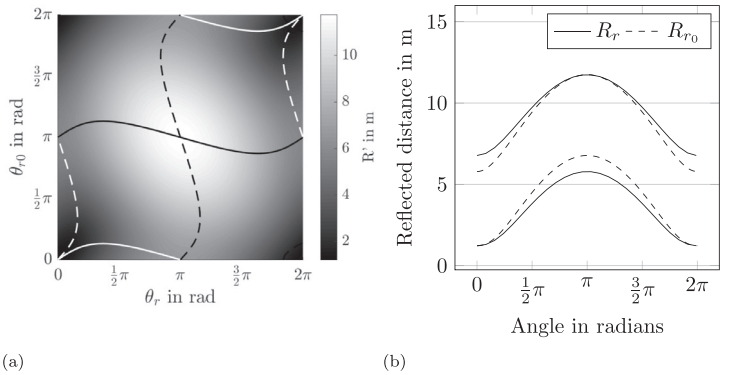

Fig. 3. (a) Reflected distance R' of two defined points when altering either of their angle coordinate θ; (b) Respective minimum and maximum distances $R'_{r,\max}(\theta_{r_0})$, $R'_{r,\min}(\theta_{r_0})$, $R'_{r_0,\max}(\theta_r)$ and $R'_{r_0,\min}(\theta_r)$.

orders from 0 to 500 using 5000 integration points. This computation is then used as a reference to determine the specific minimum number of Fourier Transform points $n_{\mathrm{FFT},r}$ for each pair $(c_{s,r}, c_{o,r})$ to achieve convergence. The condition for the evaluation of the convergence is a relative error not exceeding 10^{-2} for all Fourier coefficients whose value is at least 1% of the maximum Fourier coefficient. These parameter triplets $(n_{\mathrm{FFT},r}, c_{s,r}, c_{o,r})$ are finally used in a curve fitting procedure. The found expression is similar to the one found in [14].

$$n_{\mathrm{FFT},r}(c_{s,r}, c_{o,r}) = 8.45\left(c_{s,r} + \frac{c_{o,r}}{2\pi}\right)^{0.95} + 5 \tag{29}$$

Since the dependency of $G_r(\mathbf{r}, \mathbf{r_0})$ is the same on both angles, the expression of $n_{\mathrm{FFT},r_0}(c_{s,r_0}, c_{o,r_0})$ has to be of the same form. To enable the use of the fast radix-2 FFT algorithm, the next higher number that is a power of two should be used. Wider ranges for $c_{s,r}$ ([1, 1100]) and $c_{o,r}$ ([0,2000]) have been studied afterwards to evaluate the robustness of $n_{\mathrm{FFT},r}$ and n_{FFT,r_0}. The expressions of $n_{\mathrm{FFT},r}$ and n_{FFT,r_0} never underestimate the necessary number of Fourier Transform samples. However, when the steepness criterion is large, (e.g. larger than 50, which would be the case when a large body is located very close to the ground or when the observer point is far from the ground), $n_{\mathrm{FFT},r}$ and n_{FFT,r_0} start to overestimate the real value. A more complex expression has been developed to limit this overestimation,

$$n_{\mathrm{FFT},r}(c_{s,r}, c_{o,r}) = 7.5\left(c_{s,r}^{1.82} + \left(\frac{c_{o,r}}{2\pi}\right)^{1.88}\right)^{0.52} + 10 \tag{30}$$

Eq. (29) is thus optimised for solving on the boundary of an object that is under 2 m in diameter and not much closer than one centimetre to the ground. When solving for field points, Eq. (30) is likely more computationally efficient.

Fig. 4 represents $n_{\mathrm{FFT},r}(\theta_{r_0})$ and $n_{\mathrm{FFT},r_0}(\theta_r)$ for an arbitrarily chosen pair of source and observer point. This case is a representative example to show how to compute the 2D Fourier transform by computing consecutive 1D Fourier transforms. This proved to be computationally advantageous in this case due to reduced memory usage. The steps leading to the Fourier coefficients for this case are:

- find $\min(\max(n_{\mathrm{FFT},r}(\theta_{r_0})),\ \max(n_{\mathrm{FFT},r_0}(\theta_r)))$ to select first transformation direction. Here (see Fig. 4) $n_{\mathrm{FFT},r} = 52$ for $\theta_{r_0} = 0$, so select θ_r
- create θ_r from $\max(n_{\mathrm{FFT},r}(\theta_{r_0}))$ equally spaced values in $[0, 2\pi[$,

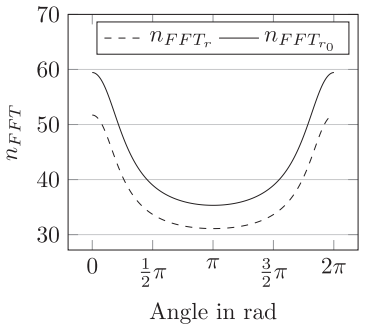

Fig. 4. n_{FFT} for different angles for the chosen example of source and receiver points.

- compute $n_{\mathrm{FFT},r_0}(\theta_r)$ for each value of θ_r and create the corresponding θ_{r_0},
- evaluate $G_r(\mathbf{r},\mathbf{r}_0)$ for each value of θ_r and its corresponding values of θ_{r_0},
- calculate the Fourier transform of $G_r(\mathbf{r},\mathbf{r_0})$ over θ_{r_0} and transform it over θ_r.

Singularities can occur in the computation of H_m and H'_m. The integration points on the line integral 27 need to be deliberately chosen to avoid this. In addition to this, a convergence study about the combination of the Fourier transform and the Gaussian quadrature for singular kernels has been made via a regularisation method, as shown in Subsection 2.2.5.

2.2.4. Discretisation process

The generator is discretised using quadratic line elements. Any point on the generator can be described by the following coordinates

$$x_0 = \mathbf{N}(\xi)\mathbf{x}_e \text{ and } r_0 = \mathbf{N}(\xi)\mathbf{r}_e \tag{31}$$

where $\mathbf{N}$ is a matrix containing the second order iso-parametric shape functions, $\mathbf{x}_e$ and $\mathbf{r}_e$ contain the nodal coordinates of the element to which $\mathbf{r_0}$ belongs and ξ is the local element coordinate. $P_m(x_0,r_0)$ and $V_m(x_0,r_0)$ can now be expressed by the same formulation

$$P_m(x_0,r_0) = \mathbf{N}(\xi)\mathbf{p}_{e_m} \tag{32}$$

$$V_m(x_0,r_0) = \mathbf{N}(\xi)\mathbf{v}_{e_m} \tag{33}$$

with $\mathbf{p}_{e_m}$ and $\mathbf{v}_{e_m}$ containing the nodal values of the corresponding element e. The line segment $\mathrm{d}l_0$ is expressed as a function of $\mathrm{d}\xi$

$$\mathrm{d}l_0 = \left\| \begin{matrix} \mathrm{d}x_0 \\ \mathrm{d}r_0 \end{matrix} \right\| = \left\| \begin{matrix} \frac{\mathrm{d}x_0}{\mathrm{d}\xi} \\ \frac{\mathrm{d}r_0}{\mathrm{d}\xi} \end{matrix} \right\| \mathrm{d}\xi = \mathrm{J}_e \mathrm{d}\xi \tag{34}$$

with the Jacobian J_e. With that, the element formulation in Eq. (27) can be written in the discretised form

$$\begin{aligned} \frac{1}{2}P_m(\mathbf{r}) &= \sum_e \left[\underbrace{-\mathrm{j}\rho\omega \int_{-1}^{1} H_m \mathbf{N}\, r_0 \mathrm{J}_e \mathrm{d}\xi}_{\mathbf{G}_{e_m}(\mathbf{r})} \mathbf{v}_{e_m} - \underbrace{\int_{-1}^{1} H'_m \mathbf{N}\, r_0 \mathrm{J}_e \mathrm{d}\xi}_{\mathbf{H}_{e_m}(\mathbf{r})} \mathbf{p}_{e_m} + \sum_p \left[\underbrace{-\mathrm{j}\rho\omega \int_{-1}^{1} H_{r_{mp}} \mathbf{N}\, r_0 \mathrm{J}_e \mathrm{d}\xi}_{\mathbf{G}_{r_{emp}}(\mathbf{r})} \mathbf{v}_{e_p} - \underbrace{\int_{-1}^{1} H'_{r_{mp}} \mathbf{N}\, r_0 \mathrm{J}_e \mathrm{d}\xi}_{\mathbf{H}_{r_{emp}}(\mathbf{r})} \mathbf{p}_{e_p} \right] \right] \\ &= \mathbf{G}_m(\mathbf{r})\mathbf{v}_m - \mathbf{H}_m(\mathbf{r})\mathbf{p}_m + \sum_p \left[\mathbf{G}_{r_{mp}}(\mathbf{r})\mathbf{v}_p - \mathbf{H}_{r_{mp}}(\mathbf{r})\mathbf{p}_p \right]. \end{aligned} \tag{35}$$

The vectors $\mathbf{p}_m$, $\mathbf{p}_p$, $\mathbf{v}_m$ and $\mathbf{v}_p$ collect the nodal values on the generator. Assembling the entries of the element matrices $\mathbf{G}_{e_m}(\mathbf{r})$, $\mathbf{H}_{e_m}(\mathbf{r})$, $\mathbf{G}_{r_{emp}}(\mathbf{r})$ and $\mathbf{H}_{r_{emp}}(\mathbf{r})$ produces the global matrices $\mathbf{G}_m(\mathbf{r})$, $\mathbf{H}_m(\mathbf{r})$, $\mathbf{G}_{r_{mp}}(\mathbf{r})$ and $\mathbf{H}_{r_{mp}}(\mathbf{r})$. P_m at any point of the generator is now linked to its amplitude at every node of the generator. A collocation scheme is used, with P_{obs} being placed successively on each node on the generator. Eq. (35) is written successively for each location, which leads to the system of equations

$$\mathcal{C}\mathbf{p}_m = \mathcal{G}_m\mathbf{v}_m - \mathcal{H}^*_m\mathbf{p}_m + \sum_p \left[\mathcal{G}_{r_{mp}}\mathbf{v}_p - \mathcal{H}^*_{r_{mp}}\mathbf{p}_p \right] \tag{36}$$

where each row of $\mathcal{G}_m$ is equal to $\mathbf{G}_m(\mathbf{r})$ evaluated at the corresponding node, and likewise for $\mathcal{H}^*_m$, $\mathcal{G}_{r_{mp}}$ and $\mathcal{H}_{r_{mp}}$. $\mathcal{C}$ is a diagonal matrix collecting the c coefficients. Since Eq. (36) yields a coupling between the Fourier coefficients P_m, it needs to be written for every circumferential order $m = [1 \ \cdots \ M]$ which results in a solvable system of equations

$$\begin{bmatrix} \mathcal{H}_{11} & \cdots & \mathcal{H}^*_{r_{1m}} & \cdots & \mathcal{H}^*_{r_{1M}} \\ \vdots & & \vdots & & \vdots \\ \mathcal{H}^*_{r_{m1}} & \cdots & \mathcal{H}_{mm} & \cdots & \mathcal{H}^*_{r_{mM}} \\ \vdots & & \vdots & & \vdots \\ \mathcal{H}^*_{r_{M1}} & \cdots & \mathcal{H}^*_{r_{Mm}} & \cdots & \mathcal{H}_{MM} \end{bmatrix} \begin{bmatrix} \mathbf{p}_1 \\ \vdots \\ \mathbf{p}_m \\ \vdots \\ \mathbf{p}_M \end{bmatrix} = \begin{bmatrix} \mathcal{G}_{11} & \cdots & \mathcal{G}_{r_{1m}} & \cdots & \mathcal{G}_{r_{1M}} \\ \vdots & & \vdots & & \vdots \\ \mathcal{G}_{r_{m1}} & \cdots & \mathcal{G}_{mm} & \cdots & \mathcal{G}_{r_{mM}} \\ \vdots & & \vdots & & \vdots \\ \mathcal{G}_{r_{M1}} & \cdots & \mathcal{G}_{r_{Mm}} & \cdots & \mathcal{G}_{MM} \end{bmatrix} \begin{bmatrix} \mathbf{v}_1 \\ \vdots \\ \mathbf{v}_m \\ \vdots \\ \mathbf{v}_M \end{bmatrix} \tag{37}$$

with $\mathcal{H}_{mm} = \mathcal{C} + \mathcal{H}^*_m + \mathcal{H}^*_{r_{mm}}$ and $\mathcal{G}_{mm} = \mathcal{G}_m + \mathcal{G}_{r_{mm}}$.

The pressure on the boundary can now be solved from Eq. (37) inserting $\mathbf{v}_m$ for $m = [1 \cdots M]$ as computed by the WFEM. Once the pressure is solved on the boundary, field points evaluation can be proceeded from

$$P^*_m(\mathbf{r}) = \mathbf{G}_m(\mathbf{r})\mathbf{v}_m - \mathbf{H}_m(\mathbf{r})\mathbf{p}_m + \sum_p \left[\mathbf{G}_{r_{mp}}(\mathbf{r})\mathbf{v}_p - \mathbf{H}_{r_{mp}}(\mathbf{r})\mathbf{p}_p \right]. \tag{38}$$

Since acoustic modes are coupled due to the reflective plane, the degree of accuracy in the computation of each one of them depends on the total number of acoustic modes solved for. This means that even if only M circumferential structural modes are excited, it might be necessary to solve for more than M circumferential acoustic modes. Thus a convergence study should be done to determine the number of circumferential acoustic modes necessary for a desired precision. This can be done simply by adding null vectors in the right hand side of Eq. 37, which corresponds to adding Fourier coefficients of the normal velocity equal to zero.

2.2.5. Regularisation of singular integrals

Singular integral kernels occur in the BE formulation during the collocation process on each element where the observer point is placed. Integrating over such kernels leads to $R \to 0$ in Eq. 15. By selecting an even number of Gauss points in the quadrature, the function is not evaluated at a singularity, instead the numerical approximation of the integral approaches the correct value with an increasing number of Gauss points. To test this, every singular kernel in the collocation scheme has been regularised by introducing a constant ϵ as follows:

$$G_{hs}(\mathbf{r}, \mathbf{r_0}) = \frac{e^{-jkR}}{4\pi (R+\epsilon)} + R_p \frac{e^{-jkR'}}{4\pi R'} \tag{39}$$

The radiated sound power has been evaluated for a monopole source using the regularised formulation and compared to the analytical model. The difference between the analytical and the BE model has been evaluated for 4, 10 and 20 points in the Gaussian quadrature, for different values of ϵ. This is shown in Fig. 5. For all three cases, the solution converges for decreasing ϵ. The difference is, expectedly, higher for a smaller number of Gauss points in the integration scheme.

Precautions have to be taken also in the computation of $\mathbf{G}_{r_{mp}}(\mathbf{r})$ and $\mathbf{H}_{r_{mp}}(\mathbf{r})$ since singular integrals arise when solving for a field point of coordinates $x = x_0$ and $r \in [-2z_{plane} - r_0, -2z_{plane} + r_0]$. Fig. 6 illustrates such a situation, where two

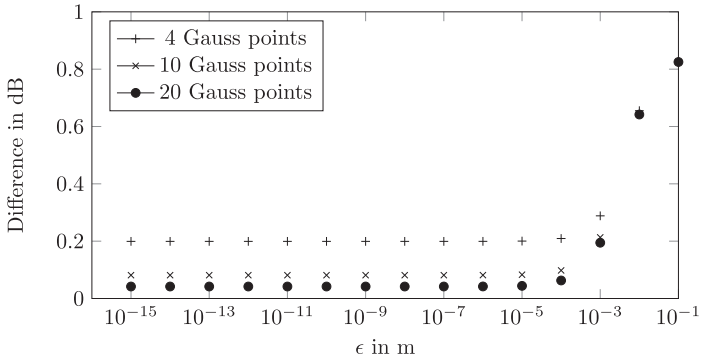

Fig. 5. Difference of the radiated sound power of a monopole source when comparing the BE model to the analytical solution, for different values of ϵ.

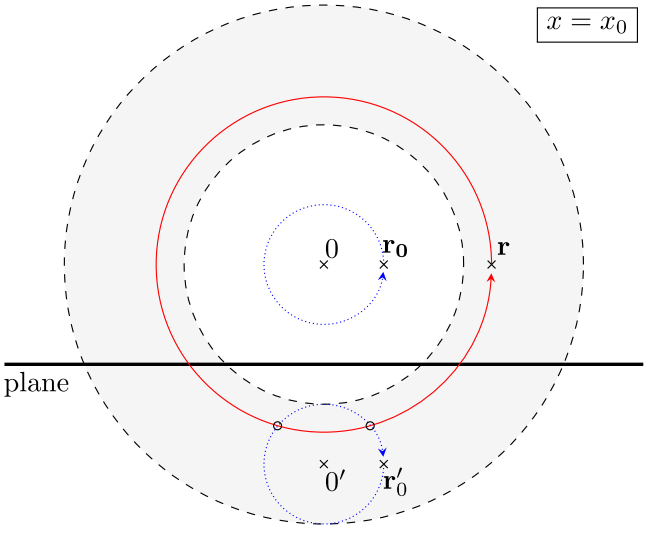

Fig. 6. Area including singularities when solving for field points, in the plane $x = x_0$. The vectors $\mathbf{r_0}$ and $\mathbf{r}$ are, respectively, the point of the generator and a field point.

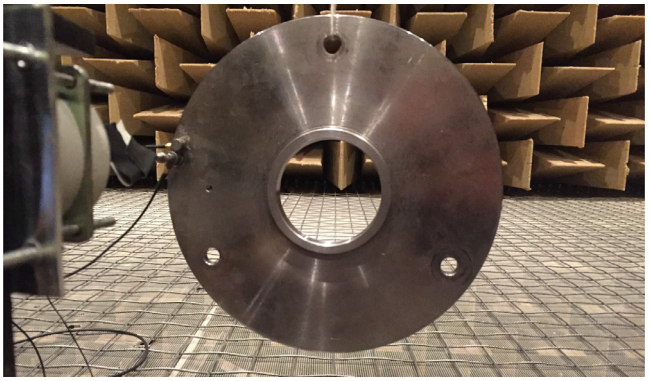

Fig. 7. Suspended disk in fully anechoic environment with shaker excitation (left) during validation measurements.

singularities occur (marked by "o"). In theses cases, when combining the 2D Fourier Transform with the line integral over the generator, $R' \to 0$ in Eq. 15. A regularisation procedure similar to the one shown for the free field singularities should be used.

2.3. Validation of the Method

The validation is conducted in two steps, a validation of the combined WFE and free-field FBEM method, and a validation of the half-space axisymmetric FBEM method. All the following results are obtained using, respectively, 4 and 20 Gauss points to compute regular and regularized singular integrals over the generator. For the first part, a directivity measurement on an axisymmetric metal disk was conducted. The disk with the outside diameter of 22 cm, a central hole with 6 cm diameter and 8 mm thickness was suspended in an anechoic environment as shown in Fig. 7. A shaker was used to apply an axial excitation at its outer diameter. The force input and acceleration at the input position were measured. A microphone was then manually positioned in 5 degree increments around the structure, where the 0 to 180 degree axis corresponds to the rotational symmetry axis of the structure. Fig. 8 shows the measured and calculated input mobility for the structure. The agreement is considered sufficient. The energy input into the structure is high at the resonance frequencies of the body. Due to the contribution of the shaker noise to the sound pressure at all frequencies, which is not included in the model, deviations of the measured and simulated sound pressure level are found, especially in proximity to the shaker. Thus, the comparison focuses on the resonance frequencies, at which the sound radiation from the structure dominates. Fig. 9 shows the comparison of the sound pressure level for some resonance frequencies. In general, these match closely. However, some shifts in angle can be observed, which might be due to imprecisions in the manual positioning. The increasingly complex radiation patterns require a higher accuracy and resolution of the positions with increasing frequencies. The second part of the validation considers the half-space formulation. Here, a numerical solution is compared to analytical models. The researched geometry is a breathing sphere. A semi-circle with $a = 1$ m diameter functions as the generator. A reflective plane is introduced with a distance of 0.51 m from the axis of rotation. To test the effect of the reflection, a reflection factor of -1 is used, effectively phase-shifting the mirror-image by π rad. The effect is shown in Fig. 10 as function of the wavenumber in air relative to the diameter of the sphere ka. For low ka, the structure follows the predicted radiation efficiency of a dipole. This is expected considering the phase relation between the sphere and its mirror image as well as the large wavelength compared to the size of the radiator. For large ka, the influence of the reflection decreases. Thus, towards high ka, the radiation efficiency approaches that of the breathing sphere.

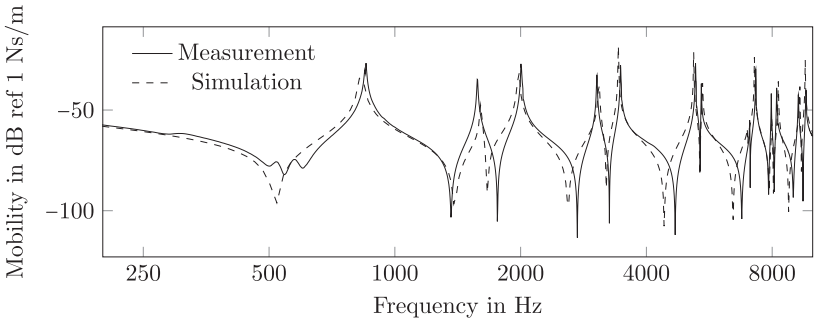

Fig. 8. Simulated and measured axial input mobility at the edge of the measured disk.

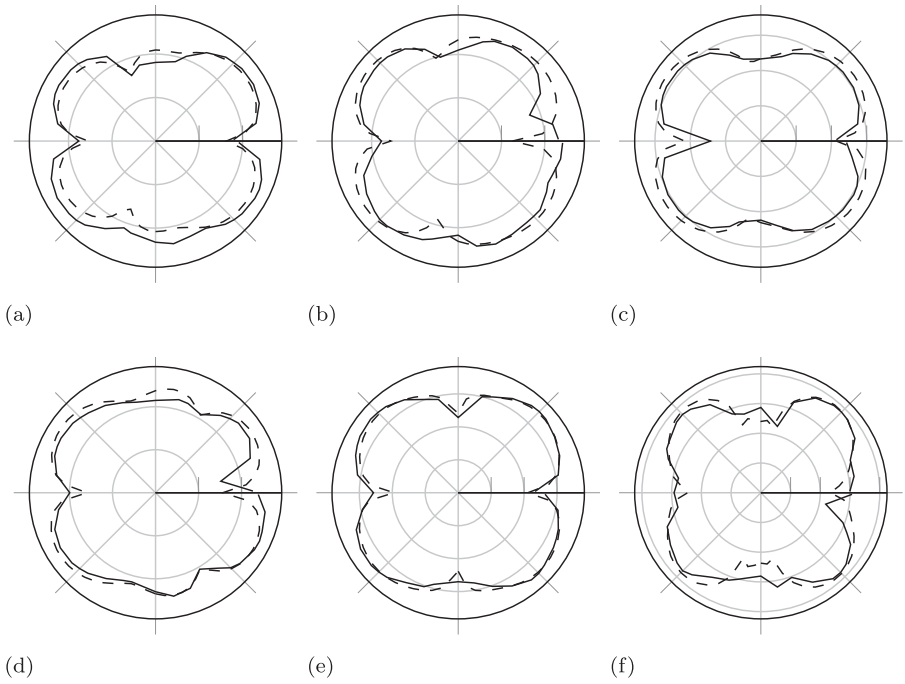

Fig. 9. Validation of the free field implementation based on a measurement in an anechoic environment. Sound pressure level in dB, where concentric grid lines correspond to 25 dB steps. (—) Simulation, (___) Measurement. (a) 864 Hz, (b) 1710 Hz, (c) 1980 Hz, (d) 2200 Hz, (e) 3040 Hz, (f) 5220 Hz.

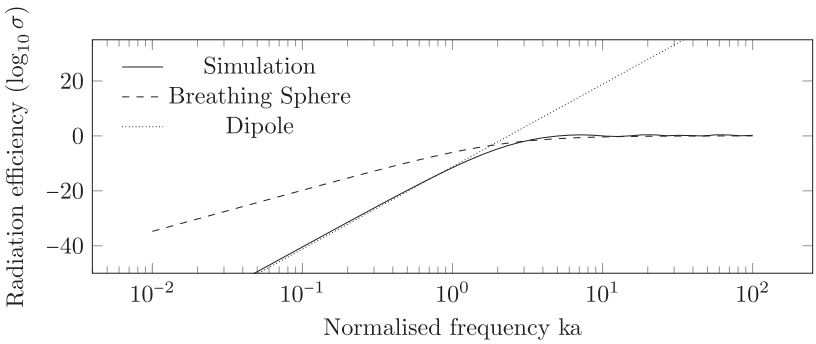

Fig. 10. Simulated and analytical solutions for the radiation efficiency.

3. Application on a railway wheel

The presented methods are applied on a common railway wheel with a straight web. The wheel geometry is of type BA093 as e.g. used in the noise measurement car (SMW) of DB Systemtechnik, described in [25]. A medium worn profile is assumed with a rolling radius of 0.47 m.

3.1. Analysis of the structural dynamics

First, the structural response of the wheel is evaluated. Fig. 11 shows the geometry and discretisation using 9-node, isoparametric, quadratic elements. As in [20], the extended geometry of the axle is neglected and a rigid connection on the wheel hub is assumed, (dashed rectangle in Fig. 11). The dispersion relation for the presented wheel is shown in Fig. 12. In the considered frequency range up to 10 kHz, 79 modes are found with up to 13 nodal diameters. Axial, radial and circumferential modes with an increasing number of nodal circles exist for each number of nodal diameters. The mobility at the contact location is also presented in Fig. 12. Expectedly, the axial mobility is mainly determined by the axial modes with a low number of nodal circles. Analogously, radial mode shapes have a dominant influence on the radial mobility. However both directions are coupled due to the non-symmetry of the wheel. The vibration behaviour below 2 kHz is dominated by the axial modes with up to four nodal diameters and up to one nodal circles (see Fig. 13a and 13b, with the first radial mode shape (Fig. 13d) occuring at 1.3 kHz.

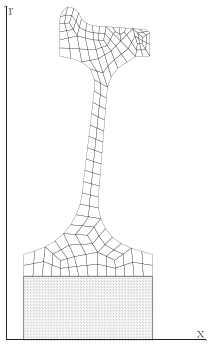

Fig. 11. The wheel geometry and FE-Mesh. The grey, dashed rectangle in the bottom represents the axle, providing a fixed constraint on the wheel hub. The x-axis is identical to the axis of symmetry.

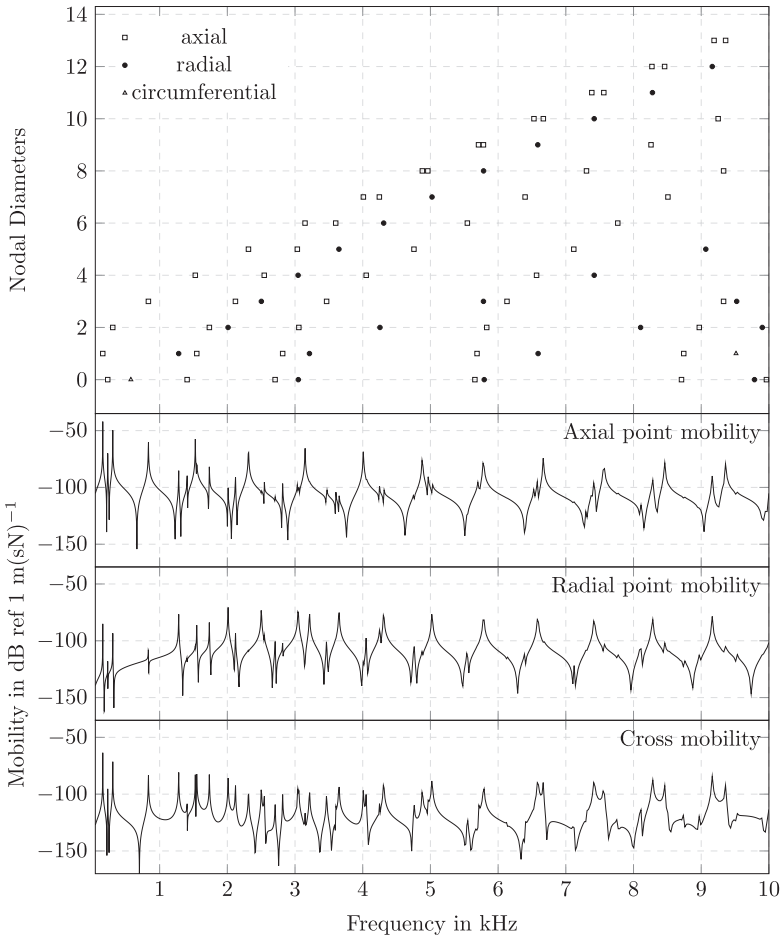

Fig. 12. Top: Dispersion relation for the SMW wheel. Marked modes are **a**(0,0,a), **b**(4,0,a), **c**(0,2,a) and **d**(1,0,r). The axial, radial and axial/radial mobility at the contact point are shown in the lower part of the figure.

3.2. Radiation ratios of the free and half-space model

The radiated sound power is evaluated for a harmonic unit force at the contact node, in axial and radial direction, respectively. An analysis similar to [20] is performed by evaluating the radiation ratio

$$\sigma = \frac{P_{rad}}{\rho_0 c_0 S \langle \overline{v^2} \rangle} \tag{40}$$

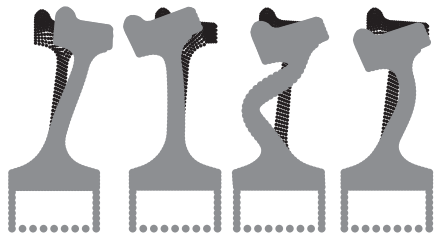

Fig. 13. The mode shapes of the modes labelled in Fig. 12. The notation is (n, m, a/r) with the number of nodal diameters n, the number of nodal circles m and the main direction of motion, axial or radial, respectively.

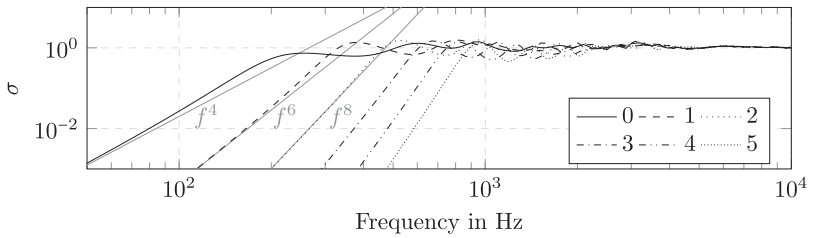

Fig. 14. Radiation ratio σ of the wheel for different numbers of nodal diameters and an axial excitation at the contact point. The slopes of functions proportional to f^4, f^6 and f^8 are included as a reference.

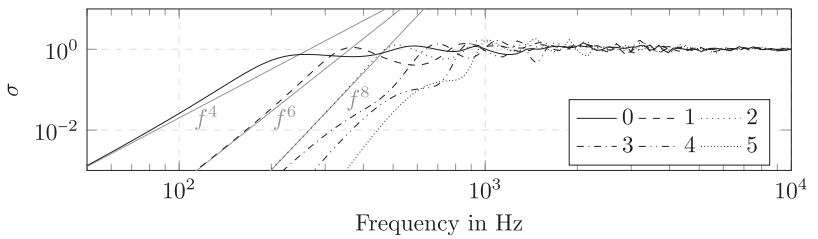

Fig. 15. Radiation ratio σ of the wheel for different numbers of nodal diameters and radial excitation at the contact point. The slopes of functions proportional to f^4, f^6 and f^8 are included as a reference.

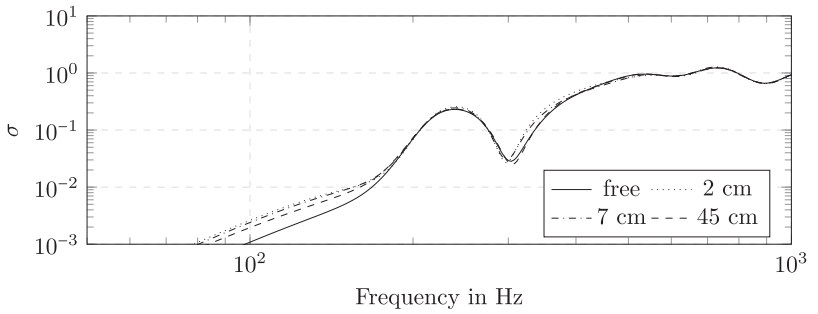

Fig. 16. Radiation ratio σ for different heights of the reflective plane. The wheel is excited radially in the contact point.

with the spatially ($\langle\rangle$) and temporally ($\overline{}$) averaged squared velocity v on the surface S, the impedance of a plane wave in air $\rho_0 c_0$ and the radiated sound power P_{rad}. The radiation ratio has been evaluated for a wheel in a free field as well as for a half space setup with the lowest point of the wheel 20 cm above an acoustically rigid ground, representing for example the wheel on a rail over a slab track. Fig. 14 shows this radiation ratio for six orders for radiation in free field and excitation in axial direction. The low-frequency radiation ratio follows the function described in [20], f^{2n+4} for order n. The behaviour of these orders can therefore be approximated by the radiation of multipoles, with σ tending towards unity once the wavelength in air is in the same magnitude or smaller than the radiating object. The radiation ratio of six orders for a radial force input is shown in Fig. 15. The first orders follow the multipole approximation described in [20] for axial modes, f^{2n+4}. This means that the radial force input produces a motion in the axial direction large enough to dominate the

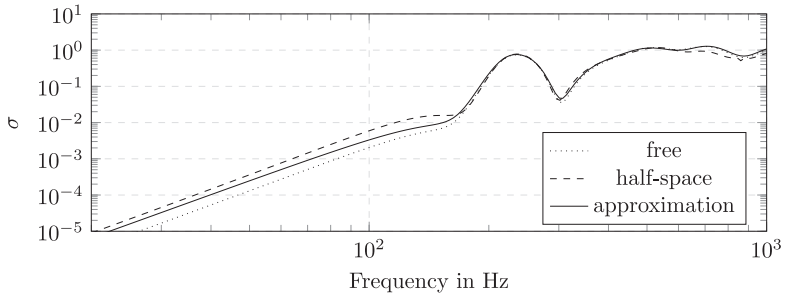

Fig. 17. Radiation ratio σ of the wheel for an axial excitation.

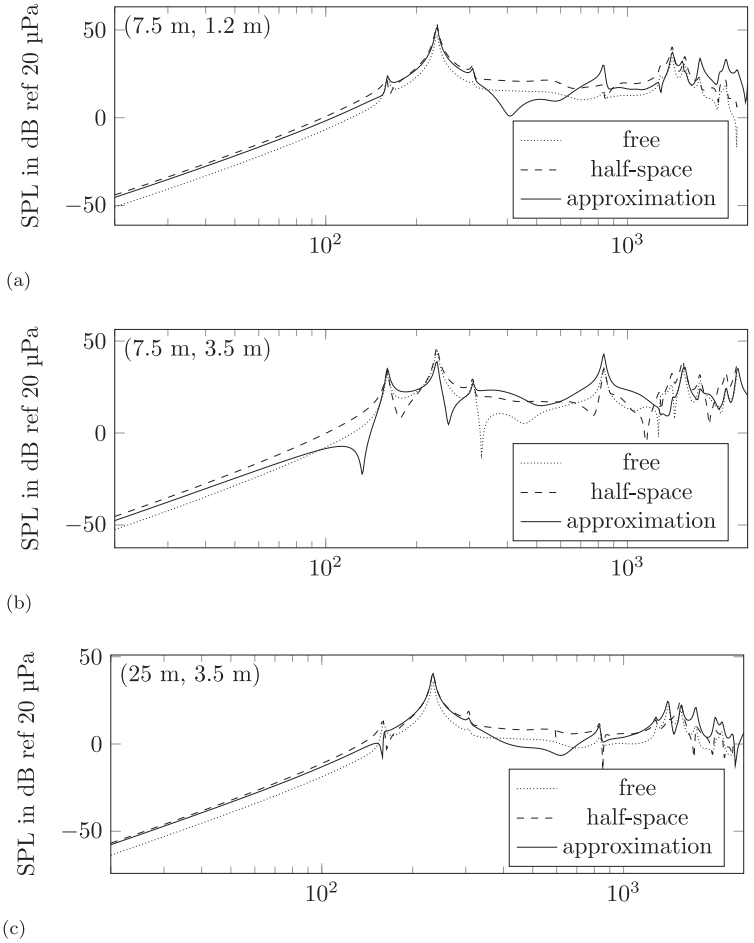

Fig. 18. Sound pressure level at three positions for a unit force axial excitation at the wheel-rail contact point. The horizontal and vertical distance from the track centre are stated in the top left.

radiation. Higher orders follow the predicted pattern of f^{2n+2} for low frequencies, meaning that for those, the radial force input leads to the dominant radiation by radial modes. Next, the half-space solution is analysed. A reflecting surface can be close to the outer diameter of the wheel, as it is the case for embedded rails for trams. For a slab track system, this distance between the top of the rail and the slab can be around 20 cm to 30 cm. An acoustically hard reflective plane ($R_p = 1$) is introduced at different heights below the wheel to quantify this effect. Due to the inherent coupling of wavenumbers in the half-space formulation, an analysis of the radiation ratio per order is not meaningful. However, the combined radiation ratio of all included nodal diameters can be compared. Fig. 16 shows this radiation ratio for a radial excitation. The influence of the plane on the radiation ratio is visible mainly at frequencies below about 170 Hz. Considering that here, the radiation ratio is below 0.01 and decreasing towards lower frequencies, the overall effect of the reflective plane is comparatively small.

3.3. Approximation of the radiation ratio by independent mirror sources

The half-space solution with a rigid reflective surface can alternatively be modelled by including a mirror source. For both the original and the mirror source, the sound pressure at a defined location can be calculated individually, without the other source present. Adding these independently calculated sound pressures can be an approximation of the solution of the coupled system.

This approximation is compared to the coupled half-space and the free-space solution of the BE model. Fig. 17 shows this comparison. In the frequency range of up to about 150 Hz, this simplification provides a better model of the radiation ratio than only using the wheel in free space. The approximation gets closer to the half-space model for lower frequencies (note that the frequency axis is shown down to 20 Hz). Above about 150 Hz, the approximation matches the radiation ratio of the wheel both in half-space and free space.

3.4. Sound pressure level at field points

As seen in the previous sections, the radiation ratio is not affected significantly by the reflective plane. However, the sound pressure level at distinct points in the sound field can see a larger impact of the reflective plane. In the following, the sound pressure level created by a unit harmonic force at the wheel-rail contact point is evaluated at three positions next to the wheel. The points are chosen according to ISO 3095 [26], assuming that the wheel is located on the rail close to the defined measurement positions.

Fig. 18 shows the evaluation of the sound pressure level at the defined field points for the wheel in free and half-space as well as for the approximation by two independent sources as described in Section 3.3. In general, the interference pattern of the sound radiated by the wheel and the reflective plane creates a sound field which is (as expected) different from that of a free wheel. For frequencies up to about 100 Hz, the expected difference of about 6 dB between the radiation in free and in half-space is visible. Here, using two independent sources for the model is an acceptable approximation. For positions (a) and (c) in the figure, the approximation is fairly close up to 300 Hz.

4. Conclusions

The purpose of this paper is to evaluate the influence of sound radiation from railway wheels over reflective planes. This is of practical interest when researching the influence of the acoustically hard surface of slab tracks on the source strength of wheel radiation. To examine this influence, the existing Fourier Boundary Element method (FBEM) has been expanded to comprise half space Green's functions. An axisymmetric formulation of the Waveguide Finite Element method (WFEM) has been used for the structural vibrations.

The proposed method of including half space Green's functions in the FBEM has been implemented and validated against numerical models. The combined model of WFEM for structural vibrations and FBEM for sound radiation showed accurate predictions when comparing to laboratory measurements of a real structure. The validated model then successfully reproduced the predictions on the radiation characteristics of a railway wheel in free field from [20]. Furthermore, it was shown that the overall radiation efficiency of a typical railway wheel is low below 150 Hz.

The effect of a reflecting plane on the source strength of a railway wheel was shown to be rather small. Consequently, the assumption used in literature (e.g. [20]) is valid above about 150 Hz. These results confirm that the models currently used to estimate the source strength from railway wheels on ballasted track are also valid approximations for wheels on slab track and even tram wheels on embedded rails.

It is further found that, even though the radiation characteristic of the wheel remains largely unchanged when introducing the reflective plane, the interference pattern of the sound radiated by the wheel and the reflective plane creates a significantly different sound field which can be observed when measuring the pressure at distinct positions. A hybrid model introduced to approximate the half-space solution was able to produce acceptable results for the source strength but could not reliably predict the sound pressure level in the sound field.

A limitation of the proposed method is the range of researched geometries. The computational cost increases for large bodies that are close to the reflective plane. The presented algorithm has been optimized for bodies in the range of about 1 m diameter and frequencies up to 10 kHz.

Declaration of Competing Interest

None.

CRediT authorship contribution statement

François Fabre: Conceptualization, Methodology, Software, Validation, Formal analysis, Writing - Original Draft. **Jannik S. Theyssen:** Conceptualization, Methodology, Software, Validation, Formal analysis, Writing - Original Draft, Writing - Review & Editing, Visualization. **Astrid Pieringer:** Supervision, Funding acquisition, Writing - review & editing. **Wolfgang Kropp:** Conceptualization, Project administration, Supervision, Resources.

Acknowledgements

The current study is part of the on-going activities in CHARMEC Chalmers Railway Mechanics (www.chalmers.se/charmec). Parts of the study have been funded within the European Unions Horizon 2020 research and innovation programme in the project In2Track2 under grant agreement No 826255.

Appendix A. Finite Element Strain Vector in cylindrical coordinates

In a cylindrical coordinate system, the strain vector is given by

$$\boldsymbol{\epsilon}(x,r,\theta) = \left(\frac{\partial u_x}{\partial x}, \quad \frac{\partial u_r}{\partial r}, \quad \frac{1}{r}\frac{\partial u_\theta}{\partial \theta} + \frac{u_r}{r}, \quad \frac{\partial u_r}{\partial x} + \frac{\partial u_x}{\partial r}, \quad \frac{\partial u_\theta}{\partial x} + \frac{1}{r}\frac{\partial u_x}{\partial \theta}, \quad \frac{\partial u_\theta}{\partial r} - \frac{u_\theta}{r} + \frac{1}{r}\frac{\partial u_r}{\partial \theta} \right)^T$$

Thus $\boldsymbol{\epsilon}$ can be expressed in term of the nodal displacement $\mathbf{u}_e$ by:

$$\boldsymbol{\epsilon} = \left(\mathbf{E}_0 + \mathbf{E}_1 \frac{\partial}{\partial \theta} \right) \mathbf{u}_e$$

with the tensor operators $\mathbf{E}_0$ and $\mathbf{E}_1$ and the vector $\mathbf{N}$ describing the cross-sectional FE shape functions

$$\mathbf{E}_0(x,r) = \begin{bmatrix} \frac{\partial}{\partial x} & 0 & 0 \\ 0 & \frac{\partial}{\partial r} & 0 \\ 0 & \frac{1}{r} & 0 \\ \frac{\partial}{\partial r} & \frac{\partial}{\partial x} & 0 \\ 0 & 0 & \frac{\partial}{\partial x} \\ 0 & 0 & \frac{\partial}{\partial r} - \frac{1}{r} \end{bmatrix} \mathbf{N}(\xi,\eta) \tag{A.1}$$

and

$$\mathbf{E}_1(x,r) = \begin{bmatrix} 0 & 0 & 0 \\ 0 & 0 & 0 \\ 0 & 0 & \frac{1}{r} \\ 0 & 0 & 0 \\ \frac{1}{r} & 0 & 0 \\ 0 & \frac{1}{r} & 0 \end{bmatrix} \mathbf{N}(\xi,\eta) \tag{A.2}$$

References

[1] O. Zienkiewicz, R. Taylor, J. Zhu, Shells as a Special Case of Three-Dimensional Analysis, in: The Finite Element Method: its Basis and Fundamentals, Butterworth-Heinemann, 2013, pp. 467–491.
[2] Dassault Systèmes Simulia, A. Fallis, D. Techniques, ABAQUS documentation, Abaqus 6.12 (2013).
[3] COMSOL, Introduction to COMSOL Multiphysics 5.3, Manual (2014).
[4] W. Kropp, F. Bécot, S. Barrelet, On the sound radiation from tyres, Acustica 86 (5) (2000) 769–779.
[5] C.-M. Nilsson, Waveguide Finite Elements Applied on a Car Tyre, Royal Institute of Technology, Stockholm, Sweden, 2004 Ph.D. thesis.
[6] C. Hoever, The simulation of car and truck tyre vibrations, rolling resistance and rolling noise, Chalmers University of Technology, 2014 Ph.D. thesis.
[7] J. Winroth, Contact stiffness in tyre / road noise modelling and speed dependencies of tyre / road noise generation mechanisms, Chalmers University of Technology, 2017 Ph.D. thesis.
[8] S. Finnveden, M. Fraggstedt, Waveguide finite elements for curved structures, Journal of Sound and Vibration 312 (4-5) (2008) 644–671.
[9] M. Ochmann, H. Brick, Acoustical Radiation and Scattering above an Impedance Plane, in: Computational Acoustics of Noise Propagation in Fluids - Finite and Boundary Element Methods, Springer Berlin Heidelberg, Berlin, Heidelberg, 2008, pp. 459–494.
[10] S.H. Schot, Eighty years of Sommerfeld's radiation condition, Historia Mathematica 19 (4) (1992) 385–401.
[11] A. Bhuddi, M.-L. Gobert, J.-M. Mencik, On the Acoustic Radiation of Axisymmetric Fluid-Filled Pipes Using the Wave Finite Element (WFE) Method, Journal of Computational Acoustics 23 (03) (2015) 1550011.
[12] A.F. Seybert, B. Soenarko, F.J. Rizzo, D.J. Shippy, A special integral equation formulation for acoustic radiation and scattering for axisymmetric bodies and boundary conditions, The Journal of the Acoustical Society of America 80 (4) (1986) 1241–1247, doi:10.1121/1.393817.
[13] W. Meyer, W. Bell, B. Zinn, M. Stallybrass, Prediction of the sound field radiated from axisymmetric surfaces., Journal of the Acoustical Society of America 65 (3) (1979) 631–638.
[14] A.H.W.M. Kuijpers, G. Verbeek, J.W. Verheij, An improved acoustic Fourier boundary element method formulation using fast Fourier transform integration, The Journal of the Acoustical Society of America 102 (3) (1997) 1394–1401.
[15] B. Soenarko, A boundary element formulation for radiation of acoustic waves from axisymmetric bodies with arbitrary boundary conditions, The Journal of the Acoustical Society of America 93 (2) (1993) 631–639.
[16] P. Juhl, An Axisymmetric Integral Equation Formulation for Free Space Non-Axisymmetric Radiation and Scattering of a Known Incident Wave, Journal of Sound and Vibration 163 (3) (1993) 397–406.
[17] P. Remington, Wheel/rail noise-Part IV: Rolling noise, Journal of Sound and Vibration 46 (3) (1976) 419–436.

[18] P.J. Remington, Wheel/rail rolling noise, I: Theoretical analysis, Journal of the Acoustical Society of America 81 (6) (1987) 1805–1823.
[19] D.J. Thompson, Wheel-rail Noise Generation, part II: Wheel Vibration, Journal of Sound and Vibration 161 (3) (1993) 401–419.
[20] D.J. Thompson, C.J. Jones, Sound radiation from a vibrating railway wheel, Journal of Sound and Vibration 253 (2) (2002) 401–419.
[21] I. Zenzerovic, Time-domain modelling of curve squeal: a fast model for one- and two-point wheel / rail contact, Chalmers University of Technology, 2017 Phd thesis.
[22] H. Brick, M. Ochmann, A half-space BEM for the simulation of sound propagation above an impedance plane, The Journal of the Acoustical Society of America 123 (5) (2008). 3418–3418
[23] X. Sheng, Y. Liu, X. Zhou, The response of a high-speed train wheel to a harmonic wheel-rail force, Journal of Physics: Conference Series 744 (1) (2016) 012145.
[24] T. Zhong, G. Chen, X. Sheng, X. Zhan, L. Zhou, J. Kai, Vibration and sound radiation of a rotating train wheel subject to a vertical harmonic wheel-rail force, Journal of Modern Transportation 26 (2) (2018) 81–95.
[25] A. Pieringer, Acoustic monitoring of rail fauls in the german railway network, 13th International Workshop on Railway Noise, Ghent, Belgium (2019).
[26] Swedish Standard Institute, Standard SFS-ISO 3095:2013. Acoustics. Railway applications. Measurement of noise emitted by railbound vehicles, 2013.